Heterogeneous ice nucleation correlates with bulk-like interfacial water

Wu, S., He, Z., Zang, J., Jin, S., Wang, Z., Wang, J., Yao, Y. and Wang, J. (2019) Heterogeneous ice nucleation correlates with bulk-like interfacial water. Science Advances, 5 (4). eaat9825. ISSN 2375-2548 doi: 10.1126/sciadv.aat9825 Available at https://centaur.reading.ac.uk/82708/

CHEMISTRY

Heterogeneous ice nucleation correlates with bulk-like interfacial water

Shuwang Wu[1], Zhiyuan He[1]*, Jinger Zang[1], Shenglin Jin[1], Zuowei Wang[2], Jianping Wang[1], Yefeng Yao[3], Jianjun Wang[1]*

Establishing a direct correlation between interfacial water and heterogeneous ice nucleation (HIN) is essential for understanding the mechanism of ice nucleation. Here, we study the HIN efficiency on polyvinyl alcohol (PVA) surfaces with different densities of hydroxyl groups. We find that the HIN efficiency increases with the decreasing hydroxyl group density. By explicitly considering that interfacial water molecules of PVA films consist of "tightly bound water," "bound water," and "bulk-like water," we reveal that bulk-like water can be correlated directly to the HIN efficiency of surfaces. As the density of hydroxyl groups decreases, bulk-like water molecules can rearrange themselves with a reduced energy barrier into ice due to the diminishing constraint by the hydroxyl groups on the PVA surface. Our study not only provides a new strategy for experimentally controlling the HIN efficiency but also gives another perspective in understanding the mechanism of ice nucleation.

INTRODUCTION

Heterogeneous ice nucleation (HIN) on surfaces exhibiting no structural resemblance to the crystal structure of ice is crucial in a variety of fields, e.g., cryopreservation of biological materials, ice formation in clouds caused by organic sea-spray aerosols, and construction of anti-icing surfaces (*1*–*9*). Although it has been recognized that interfacial water is crucial to HIN, a clear picture of how interfacial water relates to HIN has remained elusive (*10*–*18*). For example, some recent studies have shown that the extent of interfacial water layering plays an important role in HIN (*19*, *20*), whereas others have argued that this layering effect is not a useful predictor of HIN (*11*, *21*, *22*), highlighting the complexity of the role of interfacial water on HIN (*10*, *16*, *23*–*25*). It is now widely accepted that interfacial water molecules can be subdivided into different sub-ensembles, although the terminology describing the different types of interfacial water varies. For example, interfacial water molecules have been subcategorized as "tightly bound," "bound," and "free" water according to their mobility probed by nuclear magnetic resonance (NMR) (*26*, *27*). Similarly, combining thermogravimetric analysis (TGA) and differential scanning calorimetry (DSC), interfacial water molecules have been subdivided into "nonfreezable bound," "freezable bound," and "bulk" water based on their freezing behavior (*28*, *29*). Note that the above mentioned "free" or "bulk" water molecules still interact with the solid surface and are distinctly different from real bulk water. In this study, we subcategorize interfacial water molecules as "tightly bound water," "bound water," and "bulk-like water" according to their interaction strength with the hydroxyl groups of the polyvinyl alcohol (PVA) film in a strong to weak order.

Many functionalities of surfaces can be directly correlated to a specific type of interfacial water molecules, e.g., the antifouling capability of a surface is related to tightly bound water (*30*, *31*), enzymatic activity is strongly dependent on bound water (*32*, *33*), and bulk-like water plays an important role in ion exchange (*34*). However, no investigation has been carried out to correlate the HIN efficiency of surfaces with a specific type of interfacial water (*26*, *35*–*37*). Therefore, it is highly desirable to elucidate the precise role of tightly bound, bound, and bulk-like interfacial water on the HIN efficiency of a surface. In this work, we study the HIN efficiency of PVA films with controllable densities of hydroxyl groups, which can be achieved by annealing PVA films at an elevated temperature for different times. The uniqueness of PVA films is that the phase change of different types of interfacial water molecules can be accessed as PVA films have a specific thickness and contain adequate amount of interfacial water. We find that PVA surfaces with a lower hydroxyl density exhibit a higher efficiency of HIN. Further investigations with DSC and proton spin-spin relaxation time (T_2) show that the HIN efficiency on PVA surfaces shows a strong dependence on the phase change of bulk-like water. Hence, we conclude that the phase change of bulk-like interfacial water is a good predictor of the HIN efficiency of PVA surfaces.

RESULTS

Spin-coated ultrathin (~13 nm) PVA films were treated by thermal annealing. During the thermal annealing, the hydroxyl groups within the PVA films participate in chemical changes such as unsaturation, chain scission, and crosslinking (*38*), leading to an increase of the cross-link density and a decrease in the density of hydroxyl groups (in Fig. 1, A and B, and fig. S1). Figure 1C shows the x-ray photoelectron spectroscopy (XPS) results, revealing that the intensity of O1s peaks of the PVA films decreases with increasing annealing time: The carbon/oxygen (C:O) ratio increases from 2.0 (the repeat unit of PVA is -CH_2CHOH-) to 2.6, with the annealing time increased to 120 min (Fig. 1D). Meanwhile, the C:O ratios in the bulk of the PVA films are the same as those on the surface of the PVA films (fig. S2). The density of the hydroxyl groups of the PVA films can be controllably tuned by changing the annealing time, which can also be verified by the increase of the static contact angle (figs. S3 and S4). Note that the PVA/water interface morphology as well as the thickness, roughness, pore size, viscoelasticity, and crystallinity of these PVA films remain almost unchanged when the annealing time was varied from 1 to 120 min, as shown in figs. S5 to S11.

The ice nucleation efficiency of ultrathin PVA films was investigated by placing macroscopic water droplets (~400 μm of diameter) atop the PVA films and then lowering the surface temperature. An optical microscope coupled with a high-speed camera was used to investigate HIN of water droplets on differently thermally annealed PVA

[1]Institute of Chemistry, Chinese Academy of Sciences, Beijing 100190, China. [2]School of Mathematical, Physical and Computational Sciences, University of Reading, Whiteknights, Reading RG6 6AX, UK. [3]Physics Department and Shanghai Key Laboratory of Magnetic Resonance, East China Normal University, North Zhongshan Road 3663, Shanghai 200062, China.
*Corresponding author. Email: wangj220@iccas.ac.cn (J.W.); hezy@iccas.ac.cn (Z.H.)

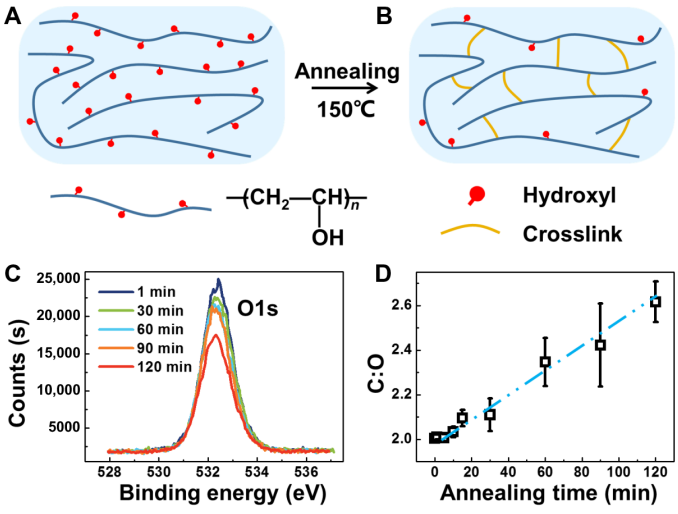

Fig. 1. PVA films with various hydroxyl densities. (**A** and **B**) Schematic illustration shows that the density of hydroxyl groups of the PVA film decreases and cross-linking between PVA chains occurs during the thermal annealing at 150°C. (**C**) XPS spectra of PVA films (recorded in ultrahigh vacuum) in the O1s region as a function of annealing time reveal a gradual reduction in the O1s signal. (**D**) The ratio of the C1s to the O1s of XPS signals of the PVA films as a function of annealing time shows the decrease of the density of hydroxyl groups as the annealing time increases from 1 to 120 min (the line is to guide the eye).

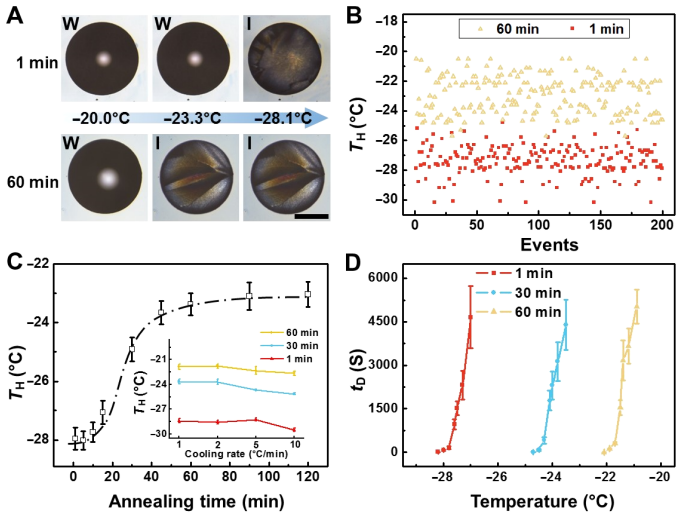

Fig. 2. Ice nucleation activity of PVA films with various hydroxyl densities. (**A**) In situ polarized optical microscopic observation of water droplet (2.0 μl) freezing on PVA surfaces annealed for 1 min (upper row) and 60 min (bottom row) at a cooling rate of 2.0°C/min. The letters "W" and "I" represent water and ice, respectively. Scale bar, 200 μm. (**B**) HIN temperature (T_H) of more than 200 individual freezing events on PVA surfaces annealed for 1 and 60 min. Each data point corresponds to one individual measurement of T_H. (**C**) T_H of water droplets on different annealed PVA surfaces and influence of the cooling rate on T_H (inset). Each data point of T_H is the mean of more than 200 independent freezing events. (**D**) Freezing delay time (t_D) of water droplets on PVA surfaces annealed for 1, 30, and 60 min under different supercoolings.

surfaces. The ice nucleation is signified by the sudden change of the opacity of water droplets, as shown in Fig. 2A and fig. S12. The water droplet atop the PVA film annealed for 1 min did not freeze until the temperature reached −28.1°C, as the temperature was lowered from room temperature (upper row images of Fig. 2A) at a rate of 2.0°C/min. In contrast, the water droplet atop the PVA surface annealed for 60 min froze at −23.3°C (bottom row images of Fig. 2A). As shown in Fig. 2B, the nucleation temperatures of more than 200 independent freezing events on each PVA surface annealed for 1 and 60 min are presented. It is obvious that the annealing time of the PVA film has a profound effect on the HIN temperature (T_H). The PVA surface annealed for 60 min exhibits a substantially higher average nucleation temperature than the one annealed for 1 min. The stability of the annealed PVA films during the HIN investigation was confirmed by atomic force microscopy (AFM) and quartz crystal microbalance with dissipation (QCM-D), as shown in figs. S8 and S13.

Figure 2C shows the change of T_H with the annealing time, and it can be concluded that T_H on PVA surfaces first increases with the annealing time and then saturates as the annealing time exceeds 60 min, exhibiting a T_H window of 5.0°C. The effect of the cooling rate on HIN was also studied (inset of Fig. 2C). When the cooling rate is larger than 2.0°C, it will affect T_H due to the heat transfer effect (fig. S14); however, under different cooling rates, T_H still follows the order of $T_{H,60min} > T_{H,30min} > T_{H,1min}$. To consolidate the efficiency of annealed PVA films on tuning HIN, we further studied the corresponding nucleation delay time (t_D) at different subzero temperatures. For the representative PVA samples with annealing times of 1, 30, and 60 min, PVA surfaces exhibit obviously distinct t_D, as shown in Fig. 2D. T_H on PVA films is independent of the molecular weight and the film thickness (from 13 nm to 20 μm) of PVA, as shown in fig. S15, indicating that, for the studied film thickness range, the effect of heating transfer on T_H is negligible. Moreover, the HIN efficiency on ultrathin PVA films with different degrees of hydrolysis (40 to 99%) was studied (fig. S16). As the density of PVA hydroxyl groups increases (the degree of hydrolysis increases from 40 to 99%), T_H decreases gradually from −21.4° ± 0.3°C to −28.0° ± 0.4°C, exhibiting a T_H window larger than 6.5°C. This finding confirms that PVA surfaces with a higher density of hydroxyl groups are more effective at depressing T_H of water.

Water molecules can penetrate into the PVA film. We compared T_H of water droplet on the surface and in the bulk of annealed PVA films, respectively, by observing the freezing of water droplets atop annealed PVA films before and after peeling off the top layer (fig. S17), which show nearly identical results. This prompted us to investigate the phase transition behavior of water molecules inside the PVA films of various annealing times. The freezing and melting behaviors of water molecules inside PVA films of various annealing times were obtained from DSC measurements. To avoid the influence of bulk water atop the surface of PVA films, the shell of PVA films was peeled off, leaving the core for the DSC investigation (film thickness of ~500 μm). As TGA detects all water molecules (including "nonfreezable water" and "freezable water") within the PVA films, while DSC measures only the freezable water within the PVA film, the difference in the number of water molecules measured by TGA and DSC is the nonfreezable water. The combined results of TGA and DSC reveal that there are nonfreezable water molecules in all PVA samples with different annealing times, as shown in fig. S18 and table S1. The nonfreezable water can be assigned to tightly bound water, in agreement with previous studies (*39*, *40*). The total water content inside PVA films decreases from 44 to 26 weight % (wt %), with the annealing time increasing from 1 to 120 min (fig. S18). The decrease in the water content with the increase of the annealing time was also confirmed by investigation with Fourier transform infrared (FTIR) absorption spectroscopy (fig. S19). Note that the minimum number of water molecules every hydroxyl groups of PVA can constrain is 2 (*37*–*39*), which can be translated to a water content of 45 wt %.

Therefore, all the water molecules inside PVA films investigated are interfacial water rather than free bulk water.

The DSC cooling curves are summarized in Fig. 3A, and the exothermal peaks correspond to the freezing of water inside the PVA film. All the cooling curves exhibit two exothermic peaks: $T_{f,a}$ (at larger supercooling) corresponding to freezing of bound water and $T_{f,b}$ (at smaller supercooling) corresponding to bulk-like water (*39*, *41*). $T_{f,a}$ decreases from −34.9° to −66.7°C, and the corresponding melting temperature of the bound water ($T_{m,a}$) decreases from −5.1° to −18.2°C as the annealing time increases from 1 to 120 min (see Fig. 3C and table S1). As the annealing time increases, the size of the formed ice crystals of the bound water may become smaller due to the effects of confinement of the PVA network. The depression of $T_{f,a}$ and $T_{m,a}$ likely stems from the size reduction of ice crystals (*42*–*44*). In contrast, $T_{f,b}$ increases from −26.8° to −19.8°C and then remains constant as the annealing time exceeds 60 min (see Fig. 3B). Note that the freezing behavior of the bulk-like water is almost the same as that of water droplets atop the PVA films (*39*, *40*, *45*). The very similar trends of $T_{f,b}$ and T_H (see Fig. 2C) indicate that HIN of water atop PVA surfaces is closely related to phase transition of the bulk-like water within the film. The melting temperatures of the bulk-like water ($T_{m,b}$) are much higher than those of the bound water ($T_{m,a}$) (Fig. 3C and fig. S20). We further evaluated the relative fraction of the bulk-like water (f_b) among all freezable interfacial water molecules from the DSC heating curves by integration and normalization of melting enthalpies (ΔH_m)

$$f_b = \frac{W_{m,b}}{W_{m,a} + W_{m,b}} = \frac{\Delta H_{m,b}}{\Delta H_{m,a} + \Delta H_{m,b}} \quad (1)$$

where W_m is the weight of water and ΔH_m is the melting enthalpies (see Fig. 3D, table S1, and Materials and Methods). The fraction of bulk-like water increases with increasing annealing time, although the total amount of interfacial water decreases, as shown in fig. S18. Note that the change of the fraction of bulk-like water with the annealing follows the same trend as that of the freezing of water droplets atop the PVA films. Both the freezing behavior and the change of the amount of interfacial water with the annealing time show that the bulk-like water correlates directly to the HIN efficiency of water atop PVA films, which can be tuned via controlling the density of the hydroxyl groups of the PVA.

To gain molecular-level insights into the correlation between the HIN efficiency and the bulk-like water, the mobility of water molecules inside PVA films of various annealing times was accessed by proton spin-spin relaxation time (T_2) measurements of water, as shown in Fig. 4 and figs. S21 and S22 (*27*, *46*–*48*). Figure 4A shows the echo decay curves, which are fitted with a biexponential function of

$$E_t = f_{2,a}\exp(-t/T_{2,a}) + f_{2,b}\exp(-t/T_{2,b}) + E_0 \quad (2)$$

which is based on the two component systems, i.e., the bound water protons (labeled "a") having a short relaxation time (T_2) and the bulk-like water protons (labeled "b") having a long T_2 (*48*, *49*). The PVA hydroxyl protons and the tightly bound water protons are not included because these are undetectable by the NMR T_2 relaxation measurement due to their extremely short T_2 (*27*). Meanwhile, bulk water atop the PVA surface was removed by blotting of the samples to exclude the influence of bulk water.

In Fig. 4B, $T_{2,a}$ and $T_{2,b}$ are both plotted against the annealing time. All values of $T_{2,a}$ fluctuate around ~20 ms, showing almost no dependence on the annealing time, whereas the value of $T_{2,b}$ increases substantially from 20 to 400 ms with increasing annealing time. Note that even the longest $T_{2,b}$ of 400 ms with an annealing time of 120 min is much smaller than the T_2 value of bulk water (~3400 ms). Therefore,

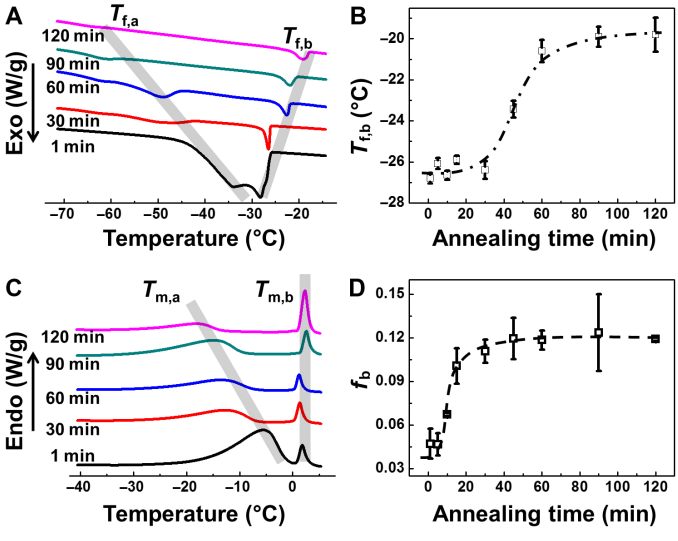

Fig. 3. Phase change behaviors of different sub-ensembles of interfacial water molecules. (**A**) DSC of freezing water molecules inside PVA films with different annealing times (thickness of film, ~500 μm). (**B**) The freezing temperature of bulk-like water with different annealing times was measured from the onset points of the DSC peaks. (**C**) DSC of melting of water molecules inside PVA films of various annealing times. (**D**) The relative fraction of the bulk-like water (f_b) among freezable waters was calculated on the basis of the enthalpies released upon the melting of bound water and bulk-like water from DSC.

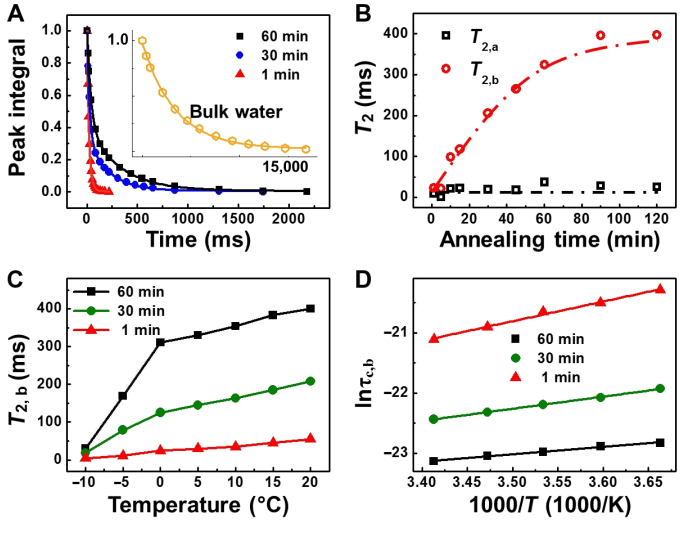

Fig. 4. The mobility of different sub-ensembles of interfacial water molecules. (**A**) T_2 decay curves of water fitted by a biexponential function for the PVA films annealed for 1, 30, and 60 min at 20°C; the inset shows the decay curve of bulk water fitted by one exponential function at 20°C. (**B**) Dependence of $T_{2,a}$ and $T_{2,b}$ on the annealing times at 20°C. (**C**) Plots of $T_{2,b}$ against the temperature for the PVA films annealed for 1, 30, and 60 min. (**D**) Plots of ln$\tau_{c,b}$ against 1000/T for the PVA films annealed for 1, 30, and 60 min.

the water with $T_{2,b}$ investigated here is affected by the hydroxyl groups of the PVA and is thus the bulk-like interfacial water. The dynamics of water can be represented by the correlation time for the motion of water (τ_c) by using the Bloembergen Purcell and Pound equation as

$$\frac{1}{T_{2,b}} = \frac{C}{2}\left(3\tau_{c,b} + \frac{5\tau_{c,b}}{1+\omega_0^2\tau_{c,b}^2} + \frac{2\tau_{c,b}}{1+4\omega_0^2\tau_{c,b}^2}\right) \quad (3)$$

where C is a constant for water of 5.33×10^9 s^{-2} and ω_0 is the Larmor frequency (*50*). The larger the value of $T_{2,b}$ (or the smaller the value of $\tau_{c,b}$) is, the faster the mobility of bulk-like interfacial water is (*27*). $\tau_{c,b}$ value decreases from 1.9 to 0.09 ns when the annealing time increases from 1 to 120 min, which indicates that the mobility of interfacial water molecules enhances as the density of hydroxyl groups of the PVA films decreases.

$T_{2,b}$ of water with different annealing times is also plotted as a function of temperature, as shown in Fig. 4C. The decrease in $T_{2,b}$ as the temperature is lowered to −5°C is caused by the freezing of bulk-like interfacial water due to the long acquisition time needed to record T_2. The temperature dependence of $T_{2,b}$ further indicates that $T_{2,b}$ represents the mobility of the bulk-like interfacial water, because the melting temperatures of bound water ensembles are all lower than −5°C (see Fig. 4D and table S1). For PVA samples annealed for 1, 30, and 60 min, the increase in temperature leads to a longer $T_{2,b}$, following the order of $T_{2,b.60min} > T_{2,b.30min} > T_{2,b.1min}$ in the temperature range of −5.0° to 20.0°C. The motion of the bulk-like water is thermally activated, which follows the Arrhenius activation law

$$\tau_{c,b} = \tau_{0,b} e^{E_{A,b}/kT} \quad (4)$$

where $E_{A,b}$ represents the activation energy and $\tau_{0,b}$ is the Arrhenius coefficient (*27*, *51*). $E_{A,b}$, which can be extracted from the fitting plots, reflects the formation and breakage of hydrogen bonds between bulk-like interfacial water molecules (Fig. 4D) (*27*, *51*). For PVA samples annealed for 1, 30, and 60 min, $E_{A,b}$ is 27.1, 16.6, and 10.2 kJ/mol, respectively. It was reported that the activation energy is ~8.6 kJ/mol for the bulk water of the phosphate-buffered saline aqueous solution (*27*); therefore, the variation of the activation energies indicates that bulk-like interfacial water molecules can rearrange themselves into favorable configurations with a lower energy barrier as the density of hydroxyl groups of the PVA films decreases (*27*). However, for the ice formation in bulk water, ice nucleation only occurs homogeneously because no foreign interfaces exist.

CONCLUSION

In summary, we investigated the freezing of water droplets atop PVA films with various densities of hydroxyl groups and found that the ice nucleation temperature increases with decreasing PVA hydroxyl group density. This unexpected finding of HIN did not stem from the PVA/water interface morphology, roughness, pore size, viscoelasticity, crystallinity, and hydrophobicity. Because water molecules can penetrate into the swollen PVA film, the interfacial water is interconnective from atop and within PVA films. This study subcategorizes the interfacial water into tightly bound water, bound water, and bulk-like water. The same trend of the HIN temperature (T_H) and the freezing temperature of bulk-like water ($T_{f,b}$) indicate the intrinsic connection of HIN of water atop PVA surfaces and the phase change of the bulk-like water within the PVA film. By tuning the density of hydroxyl groups, the ice-nucleating properties of PVA film can thus be controlled. Specifically, a reduced number of hydroxyl groups of the film give rise to more mobile bulk-like interfacial water molecules that can be more easily phase-changed into ice-like structure, thereby triggering the nucleation of a continuous water phase in contact with the film.

MATERIALS AND METHODS

Sample preparation and characterization

PVA [weight-average molecular weight (M_w) of 31 to 50 kDa; degree of hydrolysis of 98 to 99%; Aldrich] and PVA (M_w of 31 to 50 kDa; degree of hydrolysis of 40 to 99%; Kuraray) were purified with Milli-Q water and then precipitated in acetone. The precipitated PVA samples were dried in an oven at 60°C for 48 hours to remove the residual water and acetone. PVA films were prepared by spin-coating PVA aqueous solution (1% weight fraction) onto silicon wafers. The spin-coated PVA (degree of hydrolysis of 98 to 99%) films were annealed at 150.0°C for 1, 5, 10, 15, 30, 45, 60, 90, and 120 min. After the different thermal cross-linking processes, the variation of the C:O ratio, which reflects the density of PVA hydroxyl groups, was determined by XPS. The equilibrium water content of PVA films with different thermal annealing histories was determined by the TGA and weighing method. The thickness of the as-cast PVA films was about 13 nm and was detected with an ellipsometer. The surface morphology and roughness were characterized by AFM. The surface wettability was characterized by measuring the static, advancing, and receding contact angles. The crystallinity degrees of PVA ultrathin films were obtained from attenuated total reflectance FTIR (ATR-FTIR) spectroscopy. The interfacial water structure in the bulk of the film was detected with conventional FTIR absorption spectroscopy. FTIR difference spectra of different PVA surfaces were obtained under a relative humidity of 98% against the same surface under a relative humidity of 0%.

Water freezing procedure

The HIN temperature (T_H) and freezing delay time (t_D) were investigated using an optical microscope coupled with a high-speed camera (Phantom v7.3) when all the samples were placed inside a closed cell atop a cryo-stage (Linkam THMS600). The temperature resolution is 0.1°C, and the time resolution is 1.0 ms, i.e., 1000 frames/s, respectively. t_D of ice nucleation, which is defined as the time interval between the time when the surface reached an object temperature and that when the freezing happened, was measured at different supercoolings in sealed cells with a relative humidity of 100% (*6*). All the results of T_H and t_D are the mean of more than 200 independent freezing events for each PVA surface, and the error bars are the SEM. The distribution of T_H was also consolidated by Student's t test when appropriate.

DSC measurements

The crystallization and subsequent melting behaviors of water inside different annealed PVA films were performed on a calorimeter (PE DSC8000) under nitrogen atmosphere at a cooling/heating rate of 20.0°C/min. The heat flow and temperature were calibrated by pure indium before the experiments. To avoid the influence of free water on the PVA film surface, the shells of the PVA films were peeled off, leaving the core for testing. The relative amount of bulk-like water (f_b) can be calculated as $\frac{W_{m,b}}{W_{m,a}+W_{m,b}} = \frac{\Delta H_{m,b}}{\Delta H_{m,a}+\Delta H_{m,b}}$, where W is the amount of water and ΔH is the enthalpy of ice melting.

NMR measurements for water in different annealed PVA samples

The proton spin-spin relaxation time (T_2) measurements of water in different annealed PVA films were carried out on a Bruker AV600 NMR spectrometer using the Carr-Purcell-Meiboom-Gill pulse sequence. A spacing of 1.2 ms between the 90° and 180° pulse was used, and a relaxation delay of five times of the spin-lattice relaxation time between consecutive scans was necessary to ensure full recovery of the magnetization between acquisitions. The annealed PVA films were rolled and stuffed in the NMR test tube, which was filled with H_2O and D_2O (volume ratio of 1:1). All the T_2 relaxation behaviors for the water proton were fitted with a biexponential decay curve. T_2 of water was also measured as a function of temperature in a wide range from −10.0° to 20.0°C.

SUPPLEMENTARY MATERIALS

Supplementary material for this article is available at http://advances.sciencemag.org/cgi/content/full/5/4/eaat9825/DC1

Fig. S1. C1s regions of XPS data for different polymeric monomer structures.
Fig. S2. The C:O ratios detected by XPS on the surface and in the bulk of PVA film.
Fig. S3. The contact angle of samples annealed for different times at room temperature.
Fig. S4. The contact angle of samples annealed for different times at −20°C.
Fig. S5. The surface morphology of PVA films detected by AFM.
Fig. S6. The surface morphology of PVA films detected by AFM in aqueous solution.
Fig. S7. The Brunauer-Emmett-Teller results of PVA film annealed for 1, 30, and 60 min.
Fig. S8. Data of the changes of frequency (ΔF) and dissipation (ΔD) of PVA samples with annealing times detected by QCM-D.
Fig. S9. The average surface roughness (R_a) of PVA films with different annealing times.
Fig. S10. Thickness of PVA films with different annealing times.
Fig. S11. The degree of crystallinity of PVA ultrathin films.
Fig. S12. Freezing process of individual water droplet on PVA surfaces.
Fig. S13. AFM images of samples annealed for 0, 1, and 5 min before and after droplet freezing experiments.
Fig. S14. T_H of water droplets on PVA samples with different cooling rate.
Fig. S15. T_H of water droplets on PVA samples with different thicknesses and molecular weights.
Fig. S16. T_H of water droplets on PVA samples with different degrees of hydrolysis.
Fig. S17. T_H of water droplets on PVA before and after peeling off the top surface.
Fig. S18. The equilibrium water content of PVA with different thermal histories.
Fig. S19. FTIR investigation of water molecules inside the PVA films.
Fig. S20. DSC melting curve of pure water.
Fig. S21. Fitting results with a biexponential function.
Fig. S22. The plot of $\ln E_t$ versus t based on the single exponential function.
Table S1. Data from DSC.
References (*52*–*55*)

REFERENCES AND NOTES

1. A. P. Esser-Kahn, V. Trang, M. B. Francis, Incorporation of antifreeze proteins into polymer coatings using site-selective bioconjugation. *J. Am. Chem. Soc.* **132**, 13264–13269 (2010).
2. K. Liu, C. Wang, J. Ma, G. Shi, X. Yao, H. Fang, Y. Song, J. Wang, Janus effect of antifreeze proteins on ice nucleation. *Proc. Natl. Acad. Sci. U.S.A.* **113**, 14739–14744 (2016).
3. T. W. Wilson, L. A. Ladino, P. A. Alpert, M. N. Breckels, I. M. Brooks, J. Browse, S. M. Burrows, K. S. Carslaw, J. A. Huffman, C. Judd, W. P. Kilthau, R. H. Mason, G. McFiggans, L. A. Miller, J. J. Nájera, E. Polishchuk, S. Rae, C. L. Schiller, M. Si, J. V. Temprado, T. F. Whale, J. P. S. Wong, O. Wurl, J. D. Yakobi-Hancock, J. P. D. Abbatt, J. Y. Aller, A. K. Bertram, D. A. Knopf, B. J. Murray, A marine biogenic source of atmospheric ice-nucleating particles. *Nature* **525**, 234–238 (2015).
4. M. J. Kreder, J. Alvarenga, P. Kim, J. Aizenberg, Design of anti-icing surfaces: Smooth, textured or slippery? *Nat. Rev. Mater.* **1**, 15003 (2016).
5. L. Lupi, R. Hanscam, Y. Qiu, V. Molinero, Reaction coordinate for ice crystallization on a soft surface. *J. Phys. Chem. Lett.* **8**, 4201–4205 (2017).
6. Z. He, W. J. Xie, Z. Liu, G. Liu, Z. Wang, Y. Q. Gao, J. Wang, Tuning ice nucleation with counterions on polyelectrolyte brush surfaces. *Sci. Adv.* **2**, e1600345 (2016).
7. G. Graeber, T. M. Schutzius, H. Eghlidi, D. Poulikakos, Spontaneous self-dislodging of freezing water droplets and the role of wettability. *Proc. Natl. Acad. Sci. U.S.A.* **114**, 11040–11045 (2017).
8. T. M. Schutzius, S. Jung, T. Maitra, P. Eberle, C. Antonini, C. Stamatopoulos, D. Poulikakos, Physics of icing and rational design of surfaces with extraordinary icephobicity. *Langmuir* **31**, 4807–4821 (2015).
9. T. Vasileiou, T. M. Schutzius, D. Poulikakos, Imparting icephobicity with substrate flexibility. *Langmuir* **33**, 6708–6718 (2017).
10. Y. Qiu, N. Odendahl, A. Hudait, R. Mason, A. K. Bertram, F. Paesani, P. J. DeMott, V. Molinero, Ice nucleation efficiency of hydroxylated organic surfaces is controlled by their structural fluctuations and mismatch to ice. *J. Am. Chem. Soc.* **139**, 3052–3064 (2017).
11. Y. Bi, R. Cabriolu, T. Li, Heterogeneous ice nucleation controlled by the coupling of surface crystallinity and surface hydrophilicity. *J. Phys. Chem. C* **120**, 1507–1514 (2016).
12. B. Glatz, S. Sarupria, Heterogeneous ice nucleation: Interplay of surface properties and their impact on water orientations. *Langmuir* **34**, 1190–1198 (2018).
13. R. Pandey, K. Usui, R. A. Livingstone, S. A. Fischer, J. Pfaendtner, E. H. G. Backus, Y. Nagata, J. Fröhlich-Nowoisky, L. Schmüser, S. Mauri, J. F. Scheel, D. A. Knopf, U. Pöschl, M. Bonn, T. Weidner, Ice-nucleating bacteria control the order and dynamics of interfacial water. *Sci. Adv.* **2**, e1501630 (2016).
14. P. Pedevilla, S. J. Cox, B. Slater, A. Michaelides, Can ice-like structures form on non-ice-like substrates? The example of the K-feldspar microcline. *Phys. Chem. C Nanomater. Interfaces* **120**, 6704–6713 (2016).
15. G. C. Sosso, G. A. Tribello, A. Zen, P. Pedevilla, A. Michaelides, Ice formation on kaolinite: Insights from molecular dynamics simulations. *J. Chem. Phys.* **145**, 211927 (2016).
16. G. C. Sosso, J. Chen, S. J. Cox, M. Fitzner, P. Pedevilla, A. Zen, A. Michaelides, Crystal nucleation in liquids: Open questions and future challenges in molecular dynamics simulations. *Chem. Rev.* **116**, 7078–7116 (2016).
17. S. A. Zielke, A. K. Bertram, G. N. Patey, Simulations of ice nucleation by kaolinite (001) with rigid and flexible surfaces. *J. Phys. Chem. B* **120**, 1726–1734 (2016).
18. X. L. Hu, A. Michaelides, Ice formation on kaolinite: Lattice match or amphoterism? *Surf. Sci.* **601**, 5378–5381 (2007).
19. L. Lupi, A. Hudait, V. Molinero, Heterogeneous nucleation of ice on carbon surfaces. *J. Am. Chem. Soc.* **136**, 3156–3164 (2014).
20. L. Lupi, V. Molinero, Does hydrophilicity of carbon particles improve their ice nucleation ability? *J. Phys. Chem. A* **118**, 7330–7337 (2014).
21. S. J. Cox, S. M. Kathmann, B. Slater, A. Michaelides, Molecular simulations of heterogeneous ice nucleation. II. Peeling back the layers. *J. Chem. Phys.* **142**, 184705 (2015).
22. S. J. Cox, S. M. Kathmann, B. Slater, A. Michaelides, Molecular simulations of heterogeneous ice nucleation. I. Controlling ice nucleation through surface hydrophilicity. *J. Chem. Phys.* **142**, 184704 (2015).
23. S. J. Cox, Z. Raza, S. M. Kathmann, B. Slater, A. Michaelides, The microscopic features of heterogeneous ice nucleation may affect the macroscopic morphology of atmospheric ice crystals. *Faraday Discuss.* **167**, 389–403 (2013).
24. Y. Bi, B. Cao, T. Li, Enhanced heterogeneous ice nucleation by special surface geometry. *Nat. Commun.* **8**, 15372 (2017).
25. M. Fitzner, G. C. Sosso, S. J. Cox, A. Michaelides, The many faces of heterogeneous ice nucleation: Interplay between surface morphology and hydrophobicity. *J. Am. Chem. Soc.* **137**, 13658–13669 (2015).
26. P. M. Walker, C. Balmer, S. Ablett, R. A. Lerski, A test material for tissue characterisation and system calibration in MRI. *Phys. Med. Biol.* **34**, 5–22 (1989).
27. P. McConville, J. M. Pope, ^{1}H NMR T_2 relaxation in contact lens hydrogels as a probe of water mobility. *Polymer* **42**, 3559–3568 (2001).
28. E. S. Matveeva, R. Diaz Calleja, V. P. Parkhutik, Thermogravimetric and calorimetric studies of water absorbed in polyaniline. *Synth. Met.* **72**, 105–110 (1995).
29. G. Bhaskar, J. L. Ford, D. A. Hollingsbee, Thermal analysis of the water uptake by hydrocolloids. *Thermochim. Acta* **322**, 153–165 (1998).
30. J. Zheng, L. Li, S. Chen, S. Jiang, Molecular simulation study of water interactions with oligo (ethylene glycol)-terminated alkanethiol self-assembled monolayers. *Langmuir* **20**, 8931–8938 (2004).
31. E. Ostuni, R. G. Chapman, R. E. Holmlin, S. Takayama, G. M. Whitesides, A survey of structure–property relationships of surfaces that resist the adsorption of protein. *Langmuir* **17**, 5605–5620 (2001).
32. E. L. Mertz, L. I. Krishtalik, Low dielectric response in enzyme active site. *Proc. Natl. Acad. Sci. U.S.A.* **97**, 2081–2086 (2000).
33. L. Yang, J. S. Dordick, S. Garde, Hydration of enzyme in nonaqueous media is consistent with solvent dependence of its activity. *Biophys. J.* **87**, 812–821 (2004).
34. X. Liu, X. Chen, S. Pei, H. Li, Y. Zhang, Evaluation of water in perfluorinated anion exchange membranes with different IEC values. *J. Phys. Chem. C* **121**, 17546–17551 (2017).
35. W. Zhao, D. E. Moilanen, E. E. Fenn, M. D. Fayer, Water at the surfaces of aligned phospholipid multibilayer model membranes probed with ultrafast vibrational spectroscopy. *J. Am. Chem. Soc.* **130**, 13927–13937 (2008).
36. F. Xu, S. Leclerc, D. Canet, NMR relaxometry study of the interaction of water with a Nafion membrane under acid, sodium, and potassium forms. Evidence of two types of bound water. *J. Phys. Chem. B* **117**, 6534–6540 (2013).

37. M. Hishida, K. Tanaka, Long-range hydration effect of lipid membrane studied by terahertz time-domain spectroscopy. *Phys. Rev. Lett.* **106**, 158102 (2011).
38. B. Bolto, T. Tran, M. Hoang, Z. Xie, Crosslinked poly(vinyl alcohol) membranes. *Prog. Polym. Sci.* **34**, 969–981 (2009).
39. W. Li, F. Xue, R. Cheng, States of water in partially swollen poly(vinyl alcohol) hydrogels. *Polymer* **46**, 12026–12031 (2005).
40. W. G. Liu, K. D. Yao, What causes the unfrozen water in polymers: Hydrogen bonds between water and polymer chains? *Polymer* **42**, 3943–3947 (2001).
41. H. Hatakeyama, T. Hatakeyama, Interaction between water and hydrophilic polymers. *Thermochim. Acta* **308**, 3–22 (1998).
42. K. Nanjundiah, A. Dhinojwala, Melting of linear alkanes between swollen elastomers and solid substrates. *Langmuir* **29**, 12168–12175 (2013).
43. C. G. Wiener, M. Tyagi, Y. Liu, R. A. Weiss, B. D. Vogt, Supramolecular hydrophobic aggregates in hydrogels partially inhibit ice formation. *J. Phys. Chem. B* **120**, 5543–5552 (2016).
44. W. Kuhn, E. Peterli, H. Majer, Freezing point depression of gels produced by high polymer network. *J. Polym. Sci.* **16**, 539–548 (1955).
45. B.-J. Hwang, J. Joseph, Y.-Z. Zeng, C.-W. Lin, M.-Y. Cheng, Analysis of states of water in poly (vinyl alcohol) based DMFC membranes using FTIR and DSC. *J. Membrane Sci.* **369**, 88–95 (2011).
46. Y. E. Shapiro, Structure and dynamics of hydrogels and organogels: An NMR spectroscopy approach. *Prog. Polym. Sci.* **36**, 1184–1253 (2011).
47. J. Wu, S. Chen, Investigation of the hydration of nonfouling material poly(ethylene glycol) by low-field nuclear magnetic resonance. *Langmuir* **28**, 2137–2144 (2012).
48. J. Wang, M. Satoh, Water properties in a novel thermoswelling poly(vinyl alcohol) derivative hydrogel as studied by nuclear magnetic resonance and Fourier transform infrared spectroscopy. *Langmuir* **26**, 13607–13613 (2010).
49. S. Ghoshal, P. Denner, S. Stapf, C. Mattea, Study of the formation of poly(vinyl alcohol) films. *Macromolecules* **45**, 1913–1923 (2012).
50. N. Bloembergen, E. M. Purcell, R. V. Pound, Relaxation effects in nuclear magnetic resonance absorption. *Phys. Rev.* **73**, 679–712 (1948).
51. P. McConville, M. K. Whittaker, J. M. Pope, Water and polymer mobility in hydrogel biomaterials quantified by ^{1}H NMR: A simple model describing both T_1 and T_2 relaxation. *Macromolecules* **35**, 6961–6969 (2002).
52. S. K. Mallapragada, N. A. Peppas, Dissolution mechanism of semicrystalline poly (vinyl alcohol) in water. *J. Polym. Sci. B Polym. Phys.* **34**, 1339–1346 (1996).
53. N. A. Peppas, Infrared spectroscopy of semicrystalline poly(vinyl alcohol) networks. *Makromol. Chem.* **178**, 595–601 (1977).
54. G. Wypych, *Handbook of Polymers* (ChemTec Publishing, 2012).
55. C. Gurganus, A.B. Kostinski, R.A. Shaw, Fast imaging of freezing drops: No preference for nucleation at the contact line. *J. Phys. Chem. Lett.* **2**, 1449–1454 (2011).

Acknowledgments: We thank H. Lu, E. H. G. Backus, and M. Bonn for the measurements of Sum Frequency Generation spectroscopy and beneficial discussion. We also thank H. Sun and J. Wang of Bruker BNS China for the characterization of surface morphology of PVA films in water by AFM. **Funding:** We are grateful to the Chinese National Nature Science Foundation (21733010, 51436004, and 21503240) and the Strategic Priority Research Program of the Chinese Academy of Sciences (CAS) (grant no. XDA09020000).
Author contributions: Jianjun Wang initiated the idea of investigating the effect of different types of interfacial water on HIN with PVA films and supervised the experiments. S.W. and Z.H. designed and carried out the experiments except the FTIR. J.Z. carried out FTIR investigation of water molecules inside the PVA films at different annealing times. S.W., Z.H., and Jianjun Wang wrote the initial draft of the manuscript. All authors contributed to the analysis of the data and modification of the manuscript. **Competing interests:** The authors declare that they have no competing interests. **Data and materials availability:** All data needed to evaluate the conclusions in the paper are present in the paper and/or the Supplementary Materials. Additional data related to this paper may be requested from the authors.

Submitted 24 April 2018
Accepted 14 February 2019
Published 12 April 2019
10.1126/sciadv.aat9825

Citation: S. Wu, Z. He, J. Zang, S. Jin, Z. Wang, J. Wang, Y. Yao, J. Wang, Heterogeneous ice nucleation correlates with bulk-like interfacial water. *Sci. Adv.* **5**, eaat9825 (2019).

Heterogeneous ice nucleation correlates with bulk-like interfacial water

Shuwang Wu, Zhiyuan He, Jinger Zang, Shenglin Jin, Zuowei Wang, Jianping Wang, Yefeng Yao and Jianjun Wang

Sci Adv **5** (4), eaat9825.
DOI: 10.1126/sciadv.aat9825